PNAS RESEARCH ARTICLE | CELL BIOLOGY OPEN ACCESS

Single-cell RNA sequencing unveils unique transcriptomic signatures of endothelial cells and role of ENO1 in response to disturbed flow

Li-Jing Chen[a,b], Julie Yi-Shuan Li[a,b], Phu Nguyen[a,b], Ming He[c], Zhen Bouman Chen[d], Shankar Subramaniam[a,b,e], John Y.-J. Shyy[b,c,1], and Shu Chien[a,b,c,1]

Contributed by Shu Chien; received October 30, 2023; accepted December 20, 2023; reviewed by Hanjoong Jo and Huang Yu

Flow patterns exert significant effects on vascular endothelial cells (ECs) to lead to the focal nature of atherosclerosis. Using a step flow chamber to investigate the effects of disturbed shear (DS) and pulsatile shear (PS) on ECs in the same flow channel, we conducted single-cell RNA sequencing analyses to explore the distinct transcriptomic profiles regulated by DS vs. PS. Integrated analysis identified eight cell clusters and demonstrated that DS induces EC transition from atheroprotective to proatherogenic phenotypes. Using an automated cell type annotation algorithm (SingleR), we showed that DS promoted endothelial-to-mesenchymal transition (EndMT) by inducing the transcriptional phenotypes for inflammation, hypoxia responses, transforming growth factor-beta (TGF-β) signaling, glycolysis, and fatty acid synthesis. Enolase 1 (ENO1), a key gene in glycolysis, was one of the top-ranked genes in the DS-induced EndMT cluster. Pseudotime trajectory analysis revealed that the kinetic expression of ENO1 was significantly associated with EndMT and that ENO1 silencing repressed the DS- and TGF-β-induced EC inflammation and EndMT. Consistent with these findings, ENO1 was highly expressed in ECs at the inner curvature of the mouse aortic arch (which is exposed to DS) and atherosclerotic lesions, suggesting its proatherogenic role in vivo. In summary, we present a comprehensive single-cell atlas of ECs in response to different flow patterns within the same flow channel. Among the DS-regulated genes, ENO1 plays an important role in DS-induced EC inflammation and EndMT. These results provide insights into how hemodynamic forces regulate vascular endothelium in health and disease.

shear stress | endothelial cell | single-cell RNA sequencing | Enolase 1

Significance

Fluid shear stress mediates vascular homeostasis by regulating gene expression in endothelial cells (ECs). Using single-cell RNA sequencing, this study provides a comprehensive perspective of transcriptomic profiles in ECs responding to both disturbed shear (DS) and pulsatile shear (PS) in the same step flow chamber. Analyses of differentially expressed genes, biological pathways, and pseudotime trajectory revealed that DS caused EC transition from atheroprotective to atherogenic phenotypes. Specifically, DS exhibited unique transcriptomic signatures in inflammation, hypoxic responses, transforming growth factor-beta signaling, and metabolic pathways (glycolysis and lipid synthesis) to promote endothelial-to-mesenchymal transition (EndMT). Enolase 1 (ENO1) was identified to mediate DS-induced EndMT to contribute to atherosclerotic phenotype and serves as a potential therapeutic target for the prevention and treatment of vascular diseases.

There is extensive evidence that the initial pathogenic features of atherosclerosis involve the endothelial inflammatory responses induced by unsteady flow (1–4). In the straight parts of the arterial tree, where the blood flow imposes atheroprotective pulsatile laminar shear stress (PS), the vascular endothelial cells (ECs) exhibit a homeostatic phenotype. In contrast, at the inner curvature of aortic arch and bifurcations, where blood flow imposes atheroprone disturbed shear stress (DS), the ECs are dysfunctional (1, 3). In vitro studies demonstrated that DS and oscillatory shear stress (OS) with little forwarding direction cause EC dysfunction, including increases in proliferation, inflammation, permeability, oxidative stress, and endothelial-to-mesenchymal transition (EndMT). In contrast, PS maintains EC homeostasis (3). Thus, distinct flow patterns play crucial roles in determining whether the endothelium is predisposed to or protected from vascular disorders.

Previous studies by us and others using cultured ECs in the rectangular channel together with bulk RNA-seq, chromatin immunoprecipitation (ChIP)-seq, and transposase-accessible chromatin (ATAC)-seq have revealed how OS and PS differentially regulate EC gene expression at transcriptomic and epigenomic levels (5–8). For example, time-series RNA-seq data demonstrate that the OS-responsive pathways, including oxidative stress, inflammation, EndMT, and cell cycle progression, evolve over time to contribute to EC dysfunction, and that these pathways are suppressed by PS (5, 8). These bulk RNA-seq data also reveal the activation of a set of PS-induced long noncoding RNAs (lncRNAs), e.g., LINC00341 and LEENE (lncRNA enhancing endothelial nitric oxide synthase expression), which regulate VCAM1 and eNOS, respectively, to contribute to EC homeostasis (7, 9). Furthermore, bulk ChIP-seq and ATAC-seq revealed that the PS-enhanced H3K27 acetylation is enriched in the promoter region of Kruppel-like factor 4, which is a master transcription factor for EC homeostasis, leading to increased expression of inositol 1,4,5-trisphosphate receptor type 3 by altering its epigenetic state (6). These studies provide the basis for studying the transcriptomic and epigenomic regulations in the divergent EC populations by OS vs. PS.

Reviewers: H.J., Emory University; and H.Y., City University of Hong Kong.

The authors declare no competing interest.

[1]To whom correspondence may be addressed. Email: jshyy@health.ucsd.edu or shuchien@ucsd.edu.

This article contains supporting information online at https://www.pnas.org/lookup/suppl/doi:10.1073/pnas.2318904121/-/DCSupplemental.

Published January 23, 2024.

Single-cell (sc) omics technologies are the state-of-the-art methods to explore the heterogeneity of the cell populations previously assumed to be homogeneous (10–12). Through scRNA-seq (single-cell RNA sequencing) profiling of ECs from various mouse tissues, heterogeneity and unique transcriptomic signatures were identified in organ-specific ECs (11). ScRNA-seq profiling of mouse aortas has revealed EC subpopulations with distinct developmental stages and functional properties (10, 13, 14). ECs in mouse aorta respond to changes in shear stress with distinct subpopulations that exhibit different gene expressions and cell fates (15, 16). Studies of scRNA-seq and scATAC-seq in an atherogenic mouse model with DS flow induced by partial carotid ligation showed that DS changes EC transcriptomic and epigenomic profiles with an atheroprone phenotype when compared with the sham-operated carotid arteries (16). These findings demonstrated the heterogeneity and plasticity of ECs in the vascular wall, which can be regulated by a wide range of environmental cues, including hemodynamic perturbation. However, the molecular basis for the heterogeneity of ECs induced by different flow patterns and its functional ramifications remain to be determined.

ECs are not typically regarded as metabolically active and energetically demanding. However, during the onset of diseases such as atherosclerosis, pulmonary hypertension, tumor angiogenesis, and diabetes, ECs are committed to the Warburg effect in which glycolytic flux is augmented (17). Indeed, OS or DS has been shown to increase the glycolytic flux in ECs (18, 19). Enolase 1 (ENO1), catalyzing 2-phosphoglycerate to phosphoenolpyruvate, is an enzyme in the glycolytic process that has multiple functions in regulating cancer progression, including the promotion of cell proliferation, migration/invasion, inflammation, and angiogenesis (20, 21). However, the role of ENO1 in the response of ECs to shear stress has not been studied.

The aim of the present study is to investigate the impacts of DS and PS on EC at single-cell resolution by using the step flow channel. This flow device has a step change in channel height at its entrance to generate DS at the flow-reattachment region beyond the entrance, and PS is reestablished in the downstream region (22, 23). The use of the step flow channel has the advantage of studying the EC responses to DS and PS simultaneously in the same channel, in contrast to the use of the rectangular flow channel, which requires the use of two chambers to perform separate experiments on PS and OS. The paired comparison of the two flow patterns in the step flow channel increases the biological and statistical rigor. Furthermore, the step change-induced DS involves a transverse flow direction, which is an element of the flow disturbances encountered in blood vessels, and hence mimics better the in vivo flow conditions (24). Using this step flow channel in the present work, we characterized the single-cell transcriptomic signature, which demonstrated that ECs exposed to DS undergo transition from atheroprotective to atheroprone phenotype. Additionally, we have made the finding that DS induces ENO1 expression, which contributes significantly to EndMT and vascular dysfunction.

Results

DS Flow Induces Proatherogenic Responses of ECs in the Step Flow Chamber. To investigate the flow-regulated EC heterogeneity in vitro, we used the step flow channel (Fig. 1*A*) with an input PS of 12 ± 4 dyn/cm^2 to generate a DS region near the entrance and a downstream PS region. HAECs (Human Aortic Endothelial Cell) under DS and PS showed distinct morphologies, as evident by F-actin staining (Fig. 1*A*). ECs under PS presented elongated morphology with organized F-actin, whereas those under DS presented lower aspect ratio without organized F-actin. DS, in comparison to PS, significantly induced the nuclear translocation and expression of the inflammation marker NFκB-p65 at 1 h, and the augmented expression was sustained for 24 h (Fig. 1*B*), indicative of a proinflammatory response. MitoTracker staining revealed that in the PS region, 75.0 ± 1.6% of EC mitochondria existed in the tubular form (Fig. 1*C*); however, in the DS region, EC mitochondria were more fragmented, with over 67.7 ± 3.0% present in the globular form. The mitochondrial-derived ROS (mtROS) visualized by MitoSOX was significantly higher in ECs in the DS than the PS region (Fig. 1*D*). Moreover, DS increased the binucleated ECs (Fig. 1*E*) and the expression of mesenchymal marker smooth muscle protein 22α (SM22α) (Fig. 1*F*) when compared with ECs under PS, suggesting that DS promotes proliferation and EndMT of ECs. Taken together, these results demonstrated that DS, but not PS, induces proatherogenic responses in ECs.

ScRNA-seq Analysis Reveals the Transcriptomic Signatures of ECs Subjected to PS and DS. PS and DS flow patterns induce the anti- and proatherogenic phenotypes of ECs, respectively, by modulating distinct gene expressions (1, 2, 25). Analysis of scRNA-seq performed with two independent PS/DS datasets (see *Materials and Methods* section for details) showed upregulation of three PS-induced genes (KLF2, NOS3, and NQO1) in ECs in the PS region and five DS-induced genes (CAV1, CCL2, HIF1A, JUN, and MMP1) in ECs in the DS region (*SI Appendix*, Fig. S1). These results are in concert with previous studies on the regulation of EC genes by PS vs. OS (*SI Appendix*, Fig. S1) (1, 26, 27). Uniform manifold approximation and projection (UMAP) of the integrated scRNA-seq data from the two flow conditions led to the identification of eight clusters (Fig. 2*A* and *SI Appendix*, Fig. S2*A*). The distribution patterns (Fig. 2*B*) and percentages of the PS- and DS-regulated cells in these clusters were determined (Fig. 2*C* and *SI Appendix*, Table S1). The results demonstrate that the PS-regulated ECs were enriched in clusters 0, 1, 2, and 6 (with 67.2%, 81.0%, 68.9%, and 71.3%, respectively); these are defined as PS-enriched clusters. On the other hand, the DS-regulated ECs were enriched in clusters 3, 4, and 5 (with 99.7%, 98.9%, and 64.0%, respectively); these are defined as DS-enriched clusters. Although cluster 7 had a high percentage of DS-enrichment, the cell number was very low (<100) and was hence excluded from further analysis.

To functionally characterize each cluster, the cluster-specific differentially expressed genes (DEGs) were determined by comparing each cluster to all others. A heatmap for the eight clusters was generated based on the top 10 up-regulated genes in each cluster listed in *SI Appendix*, Fig. S2*C* (*SI Appendix*, Fig. S2*B*). Further ViSEAGO multiple comparisons analyses (28) with the unique DEGs ($\log_2$ fold change > 0.25) from each cluster generated a functional gene ontology (GO) heatmap, which shows GO term similarities between clusters 0 and 1, as well as clusters 3 and 4; whereas clusters 2, 5, and 6 are standalone clusters (Fig. 2*D*). Based on the GO term heatmap similarities, we defined these clusters as PS-clusters (clusters 0 and 1) and DS-clusters (clusters 3 and 4). The top GO terms in PS-clusters include vasculature development, angiogenesis, EC migration, actin cytoskeleton organization and extracellular matrix organization, which are pathways for EC homeostatic condition (*SI Appendix*, Fig. S3*A*). In contrast, the top GO terms in DS-clusters include positive regulation of cellular metabolic processes, responses to stress, cytokine and hypoxia, apoptotic process, cell differentiation and glycolytic process, which are associated with EC dysfunction leading to atherosclerotic phenotype (*SI Appendix*, Fig. S3*B*). Interestingly, clusters 2 and 6 include GO terms in both PS-clusters and

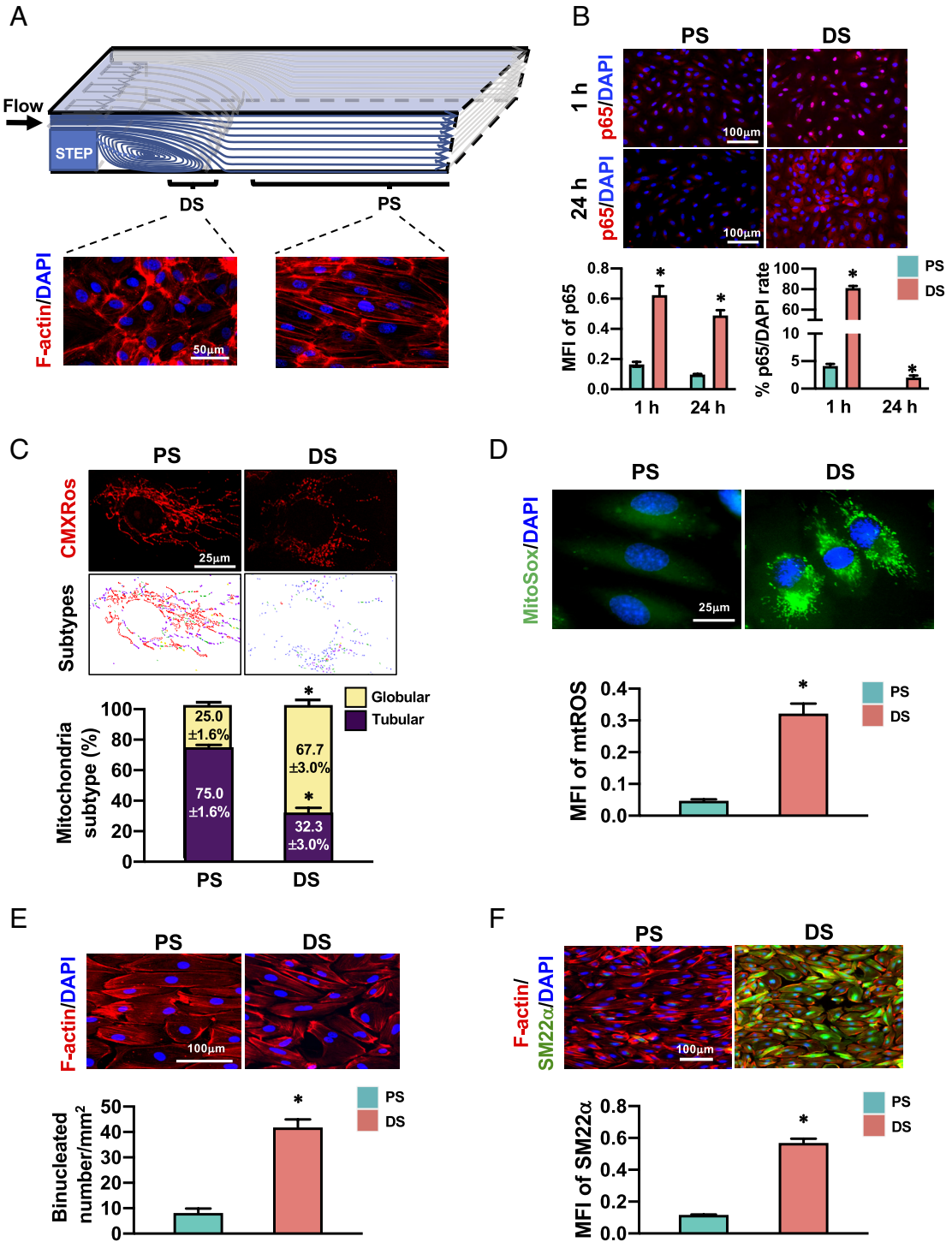

Fig. 1. DS induces EC dysfunction in the step flow chamber. (*A*) Schematic diagram of the flow patterns in the step flow chamber. (*Upper*) DS indicates the flow-reattachment region; PS indicates pulsatile laminar flow region. (*Lower*) Fluorescence staining of F-actin in ECs after exposure to DS and PS for 24 h. (*B*) Immunostaining and quantification of the expression level of p65 in ECs at PS and DS regions after 1 and 24 h of shear flow. (*C*, *Upper*) Mitochondria were stained with MitoTracker Red (CMXRos) in ECs at PS and DS regions to track the changes of mitochondrial morphology. (*Middle*) The mitochondria were classified into different subtypes based on the size of globules (blue for small globules and yellow for swollen globules) and the shape of tubules (green for linear, orange for twisted, purple for branched, and red for elongated) by MicroP analysis. (*Lower*) The percentages of globular and tubular forms of mitochondria in ECs at PS and DS regions. (*D*) Representative images and bar graph quantification of MitoSox staining of EC mitochondria ROS (mtROS) to demonstrate the production of mtROS in ECs at PS and DS regions. (*E*) Representative images and bar graph quantification of the binucleated cells in ECs at PS and DS regions. (*F*) Representative images and bar graph quantification of immunostaining of the EndMT marker SM22α in ECs at PS and DS regions after 24-h shearing in the same step flow chamber. Data represent mean ± SEM from 3 to 4 independent experiments. $^{*}P < 0.05$ for DS vs. PS. MFI: mean fluorescence intensity.

DS-clusters, i.e., adenosine triphosphate (ATP) metabolic process, apoptosis, wound healing, actin cytoskeleton organization, blood vessel development, and endothelium development (*SI Appendix*, Fig. S3 *C* and *D*). ECs in cluster 5 had high levels of gene enrichments for cell cycle, chromosome segregation, DNA repair, microtubule cytoskeleton organization, and mitotic spindle checkpoint

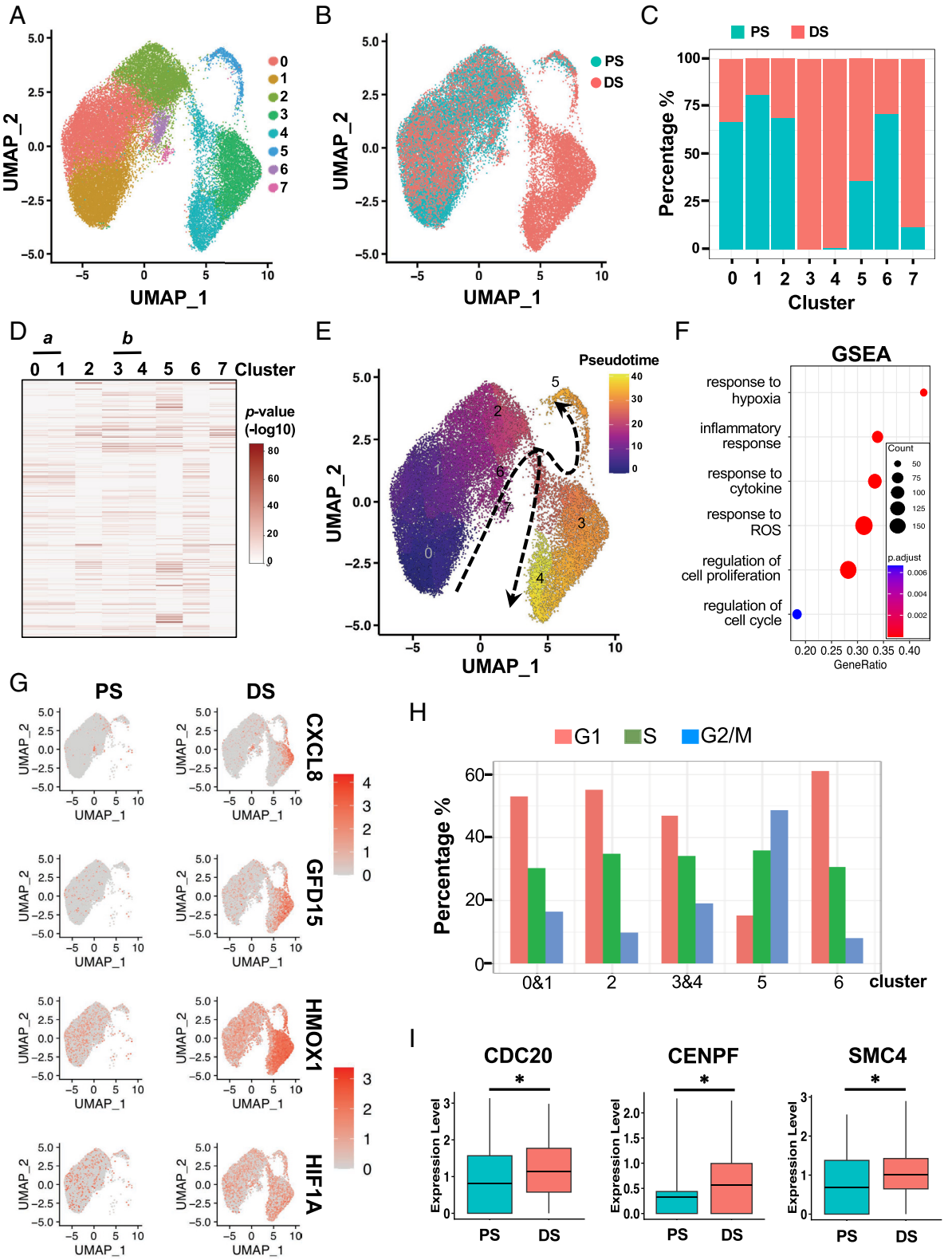

Fig. 2. Transcriptome signatures of the integrated scRNA-seq datasets in ECs subjected to PS and DS. ScRNA-seq experiments were performed on ECs collected from the DS and PS regions in the step flow chambers. (*A*) The results were plotted following data normalization, clustering, and dimensional reduction with Seurat v.4.0.2, and eight distinct clusters were identified by UMAP. (*B*) The integrated datasets were plotted to demonstrate the distributions of cells under PS (cyan) and DS (pink) by UMAP. (*C*) The percentages of cells from PS and DS regions in each of the eight clusters were quantified. (*D*) ViSEAGO multiple comparison analyses showed the heatmap of DEG functional enrichment tests of GO terms (row) in the eight cell clusters (column). Lowercase indicates a similar GO-term pattern. (*E*) ECs were color-coded for pseudotime trajectory using the Monocle3 algorithm. The arrangement of cells on the UMAP shows the path of clusters on the left side (dark purple, clusters 0 and 1) progressing to those on the right side (yellow and orange-yellow, clusters 3 to 5) over pseudotime. (*F*) GSEA plots showing that the enrichment of gene sets with response to hypoxia, inflammatory response, response to cytokine, response to ROS regulation of cell proliferation, as well as cell cycle, are significantly enriched in DS-clusters. (*G*) Feature plots showing the cells with high expression levels of inflammatory genes (CXCL8 and GDF15), sensor gene of oxidative stress HMOX1, and the hypoxia-induced master transcription factor HIF1A overlaid on the UMAP plot. (*H*) ECs were assigned to specific cell cycle phases with Seurat's CellCycleScoring function, and the percentages of the cells in the G1, S, or G2/M phase are shown for the indicated clusters. (*I*) Boxplots demonstrate the expression levels of representative G2/M phase genes (CDC20, CENPF, and SMC4) in ECs at PS and DS regions.

(*SI Appendix*, Fig. S3*E*), suggesting that these cells were in proliferative stages.

DS induction of EC Heterogeneity and Dysfunctions. To further understand the potential EC transition and plasticity status at single-cell resolution, we performed the trajectory and pseudotime analysis using the Monocle 3 package to study dedifferentiation/transitional path according to transcriptomic similarity of individual cells. The results showed the progression of a dedifferentiation/transitional path from PS-enriched clusters (clusters 0 to 2) toward clusters 3 and 4 (atheroprone phenotypes, *SI Appendix*, Fig. S3*B*) and cluster 5 (proliferative status, *SI Appendix*, Fig. S3*E*) within the increasing pseudotime (Fig. 2*E*). The GO term (*SI Appendix*, Fig. S3*B*) and trajectory analyses suggest that multiple proatherogenic responses are enriched in DS-clusters. To further demonstrate that DS induces these proatherogenic responses, the gene set enrichment analysis (GSEA) was employed to determine the significant changes of biological processes based on the DEGs in DS-clusters. GSEA dot plot (Fig. 2*F*) and correlation plots (*SI Appendix*, Fig. S4) show the positive correlation of the enriched gene sets in inflammatory response, responses to cytokine, responses to hypoxia, responses to ROS, regulation of cell proliferation, and cell cycle. Further analyses validated the augmented expression of inflammation and hypoxia/oxidative stress genes such as CXCL8, GDF15, HMOX1, and HIF1A in DS-cluster cells (Fig. 2*G*). These results reveal the molecular basis for the DS-induced EC inflammation, proliferation, and oxidative stress (Fig. 1). Next, we determined the cell-cycle scores function of each cell from Seurat. Based on the expression patterns of a panel of S phase- or G2/M phase-associated genes, each cell was assigned with a cell cycle phase. Cells not expressing these genes were assigned as being in the G1 phase (29). This analysis showed that ECs in cluster 5 exhibited marked increases in the G2/M phase in comparison to other clusters (Fig. 2*H*). DEG analysis of the transcriptomic profile of ECs in cluster 5 showed that these cells expressed higher levels of G2/M genes, such as CDC20, CENPE, and SMC4, under DS (Fig. 2*I*). These results signified the transcriptomic features of each subpopulation that demonstrate the EC heterogeneity under different flow conditions.

DS Promotes EC Plasticity and EndMT. To date, most studies used manual strategies to annotate cell types for each cluster based on DEG profile; however, it is labor intensive to accurately assign cell types and may introduce bias (30). We employed the SingleR (31) analysis tool, an automatic annotation with human primary cell atlas data reference dataset, to assign each cell with a specific cell type in the scRNA-seq datasets (Fig. 3*A*). This nonbiased analysis demonstrated that a significantly larger subpopulation of mesenchymal-like cells (MLCs, including mesenchymal stem cells, fibroblasts, smooth muscle cells, osteoblasts, embryonic stem cells and tissue stem cells) were annotated from the DS-clusters (37.08%) in comparison to the PS-clusters (5.55%) (Fig. 3 *B* and *C*). From our results on cell type annotation (Fig. 3*A*), we found only less than twenty immune cells (including bone marrow cells, B cells, B cell-CD34$^+$, and promyelocytes) in DS-clusters. Due to the limited cell numbers, these immune cells were not included for further analysis in the current study. Next, we sorted ECs from PS-clusters (PS-EC), ECs from DS-clusters (DS-EC), and MLCs from DS-clusters (DS-MLC) for further DEG analyses. Compared to PS-EC cells, 3,647 genes were differentially expressed in DS-MLCs (Fig. 3*D*) and 3,189 genes in DS-ECs. These DEGs of DS-MLC were significantly enriched for GO terms associated with myeloid cell differentiation, response to hypoxia, I-κB/NF-κB signaling, TGF-β signaling, epithelial-to-mesenchymal transition (EMT), and ATP/collagen metabolic process (Fig. 3*E*), which are associated with mesenchymal transition and development of cardiovascular diseases (32, 33). The KEGG pathway analysis demonstrates that the gene sets in cellular senescence pathway, fluid shear stress and atherosclerosis, necroptosis, apoptosis, TNF signaling pathway, and TGF-β signaling pathway were also significantly enriched in DS-MLCs (Fig. 3*F*). These results also revealed the plasticity of ECs in that DS enhances EC-MLCs transition, in agreement with their contribution to the DS-induced atheroprone phenotype.

To characterize in greater detail the transcriptomic changes for DS-MLCs transition, we focused on genes involved in mesenchymal transition, inflammation, hypoxia, TGF-β signaling, and metabolisms (glycolytic process and fatty acid metabolic process) (Fig. 3*G*). The DS-MLC group of cells showed elevated expression of genes involved in these biological characteristics. Intriguingly, DS-MLCs expressed a high level of SMAD3, whereas DS-ECs expressed a high level of SMAD1 (Fig. 3*G* TGF-β signaling panel), suggesting that the elevation of SMAD3, but not SMAD1, contributes to the DS-induced EndMT; this is consistent with the EC response to OS as report by Chen et al. (34). EC metabolism plays an important role in endothelial dedifferentiation and EndMT (35). Our results show that DS-MLCs expressed high levels of glycolytic and fatty acid metabolic enzymes such as DDIT4, ENO1, IER3, PRKAA2, and fatty acid synthase (FASN), suggesting that increases of glycolysis and fatty acid synthesis were engaged in the DS-induced mesenchymal transition. Taken together, these data indicate that the DS-induced EndMT involves the induction of inflammatory and hypoxic responses, TGF-β signaling, as well as metabolic changes, in a subpopulation of ECs.

Pseudotemporal Trajectory Analysis Revealed the Kinetic Expression of ENO1 across the EndMT Trajectory. We classified DS-cluster cell types into DS-EC, DS-MLC, and others based on the results of cell type annotation (Fig. 3*A*). To decipher the relationship between transcriptional changes and EndMT pseudotime trajectory in the DS-clusters, these cells were plotted and colored by UMAP with Seurat-based clustering (*Left*) and by pseudotime trajectory with Monocle3 analysis (Fig. 3 *H*, *Right*). The UMAP plots reveal that DS-MLCs were densely located in DS-clusters at the late pseudotime point. The boxplot quantifying the pseudotime distribution of these subpopulations shows that DS-MLCs represent the highest median of pseudotime values, suggesting that DS drove the EC-to-DS-MLC transition (Fig. 3*I*). Based on the transcriptional profile of DS-MLC, we selected the highly expressed ENO1, as well as SMAD3 and CDH2 (mesenchymal markers) in DS-MLCs to further assess the transcriptional changes associated with EndMT pseudotime. The gene expressions plotted by cell types across pseudotime revealed that the expressions of ENO1, SMAD3 and CDH2 were markedly increased, whereas that of CDH5 (EC marker) decreased, over pseudotime (Fig. 3*J*), indicating that these transcriptional changes are associated with EndMT in the DS-clusters.

ENO1 Mediates Expression of Inflammatory and EndMT Genes in ECs Responding to DS Flow. Among the DS-regulated EndMT genes, ENO1 was highly induced in the DS-MLC group (Fig. 3*G*), with the pseudotemporal trajectory in concert with the EndMT process (Fig. 3*J*). Immunostaining demonstrated that ENO1 expression in ECs was significantly higher at DS than PS region (Fig. 4*A*). En face staining of the mouse aorta arch showed that the ENO1 intensity was significantly higher at the inner curvature (DS region) than the outer curvature (PS region) (Fig. 4*B*). To investigate the role of ENO1 in the DS-induced EC inflammation

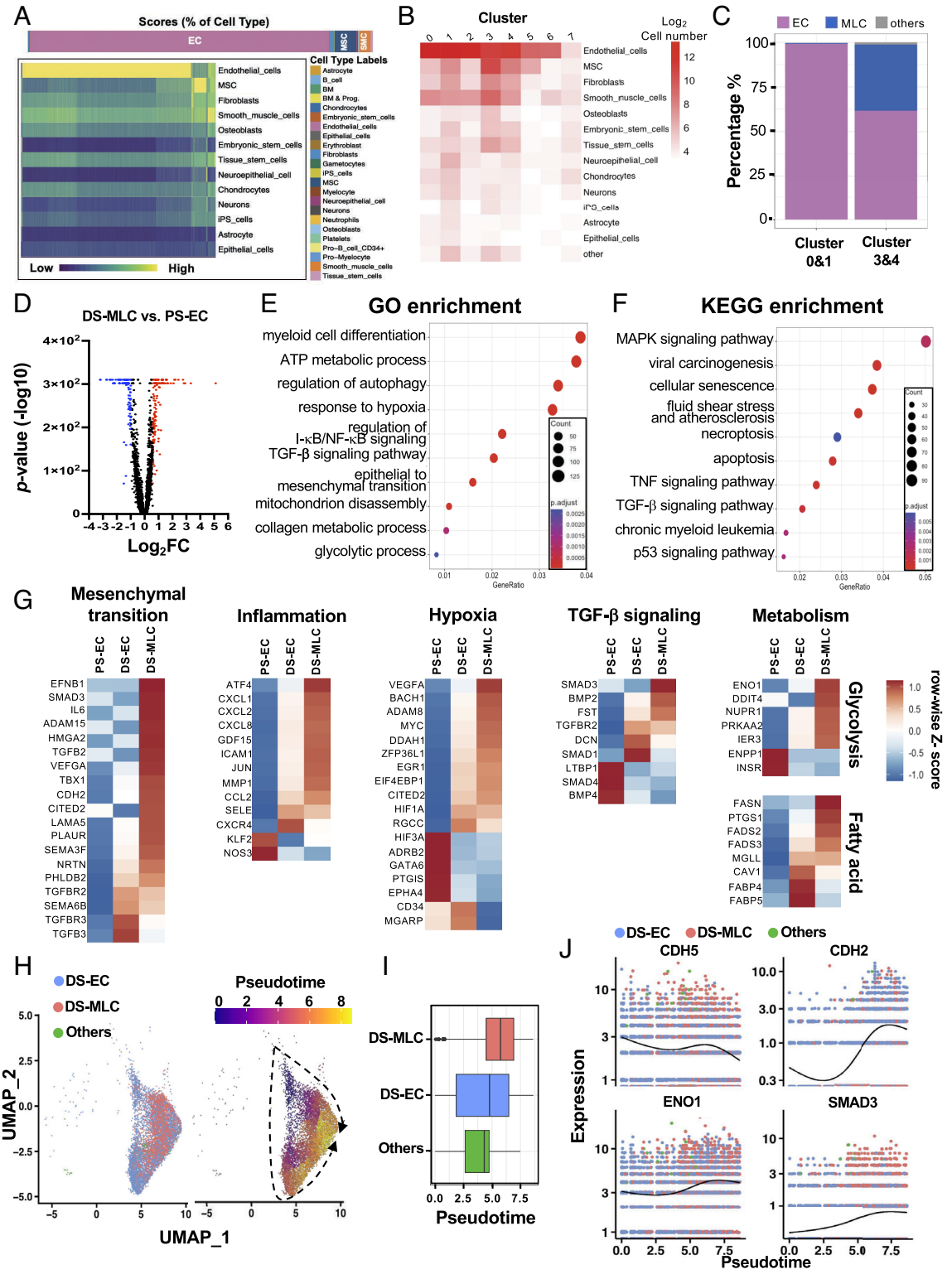

Fig. 3. The analyses of cell atlas and transcriptional profiles for DS-induced mesenchymal transition. (*A*) Each EC in scRNA-seq dataset was assigned to a specific cell type using SingleR with reference to "Human Primary Cell Atlas Data". A heatmap was generated to show the cell atlas of the cells under PS and DS. Each column represents one cell, and each row denotes the assigned cell type. The final score of each cell type in the dataset is shown on the *Top* in correspondence to the color bar on the *Right*. (*B*) The representative heatmap demonstrates the number of cells in each type. The color scale represents the $\log_2$ cell number of each cell type (row) for each cluster (column). (*C*) The stacked barplot shows the significant differences of the percentages of ECs and MLCs between PS-clusters (clusters 0 and 1) and DS-clusters (clusters 3 and 4). The significant DEGs in MLCs from DS-clusters (DS-MLC) cells were analyzed and presented with volcano plot, GO terms, and KEGG pathways using the ClusterProlifer. (*D*) In the volcano plot, the expression levels of up-regulated DEGs with $\text{Log}_2\text{FC} > 0.5$ and down-regulated DEGs with $\text{Log}_2\text{FC} < -0.5$ are highlighted in red and blue dots, respectively. The dot plots show significant enrichments of GO terms (*E*) and KEGG pathways (*F*) in DS-MLC cells. (*G*) Heatmaps of the expression levels of the genes associated with mesenchymal transition, including the gene sets related to inflammation, hypoxia, TGF-β signaling, and metabolism (glycolysis and fatty acid) in PS-EC, DS-EC, and DS-MLC datasets. (*H*) Monocle3 pseudotime trajectory analyses of the various subsets of cells in DS-clusters. The cells are labeled as DS-EC, DS-MLC, and others (*Left*) with the corresponding pseudotime trajectories (*Right*). (*I*) Boxplot showing the distribution of each cell type at pseudotime points. (*J*) Pseudotime kinetics of DS-MLC marker genes in three subtypes of cells were plotted in pseudotime points. The expression trend curves show that the increase of ENO1, SMAD3, and CDH2 expression is in concert with the increase of DS-MLCs over pseudotime, whereas that of EC marker CDH5 is not.

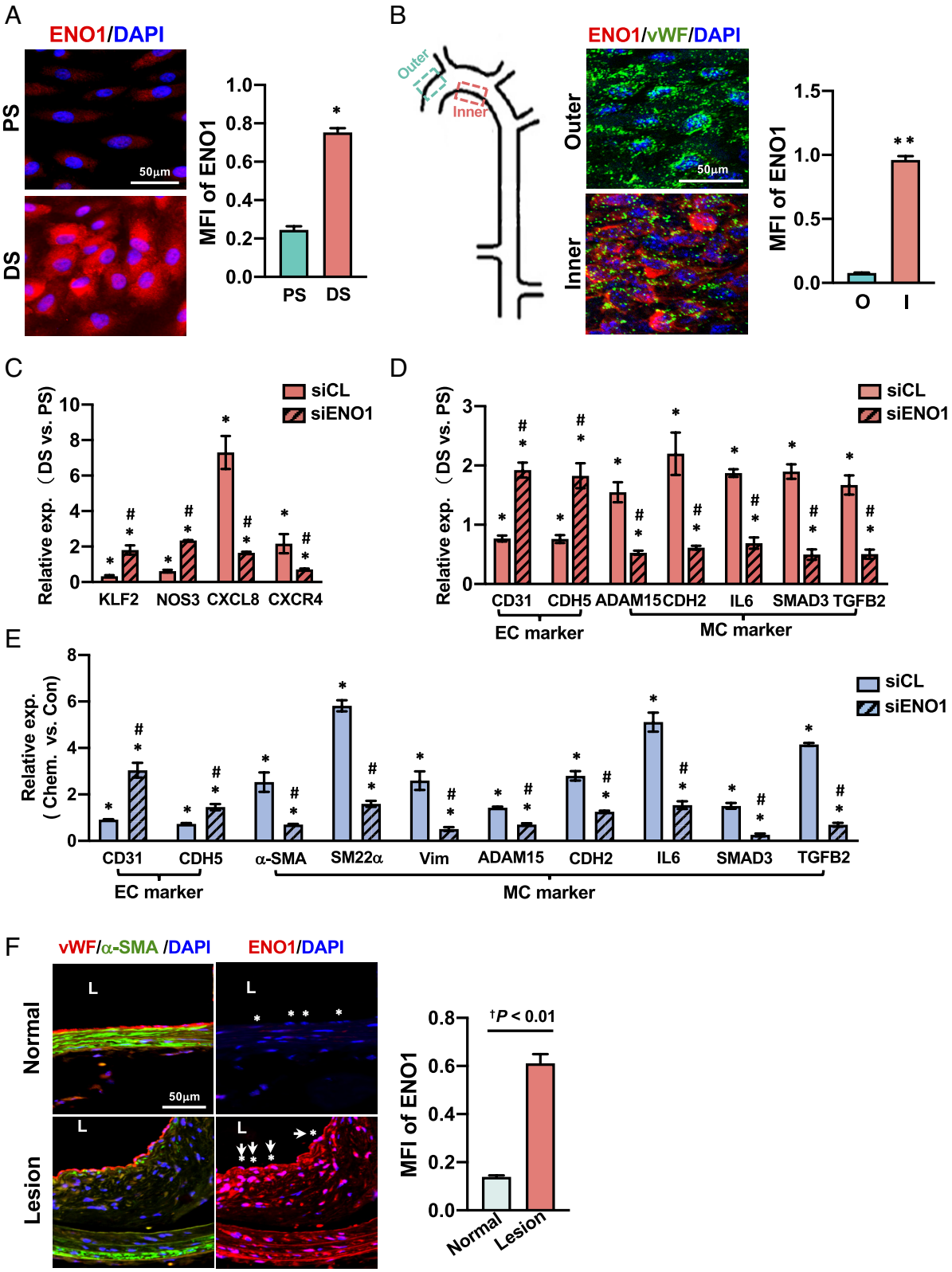

Fig. 4. DS induces ENO1 expression to mediate EC inflammatory responses and EndMT. (*A*) Representative images and bar graph quantification of ENO1 expression in ECs at PS and DS regions in the step flow chamber. (*B*) The en face coimmunostaining of ENO1 (red), vWF (green), and DAPI nuclei counterstain (blue) in ECs at the outer (O, PS region) and inner (I, DS region) curvatures of a mouse aorta arch. (*C*–*E*) ECs were transfected with 20 nM of control siRNA (siCL) or ENO1 siRNA (siENO1) for 24 h and then subjected to flows for 24 h in the step flow chamber (in *C* and *D*) or a combined treatment of 10 ng/mL TGF-β2 and 10 ng/mL IL-1β for 48 h (in *E*). Various marker genes were quantified by qPCR. (*F*) Serial cross-sections of the thoracic aorta (normal) and aortic arch (lesion) from $ApoE^{-/-}$ mice were stained with vWF (red), α-SMA (green), and ENO1 (red), as well as DAPI (blue). Stars indicate the endothelium. Arrows indicate the ENO1-positive cells. L indicates the arterial lumen. All data are representative of at least three independent experiments with mean ± SEM, $^{*}P < 0.05$ vs. PS or nontreatment. $^{**}P < 0.05$ vs. outer curvature. $^{\#}P < 0.05$ vs. siCL. $^{\dagger}P < 0.05$ vs. normal (TA). MFI: mean fluorescence intensity.

and EndMT, ENO1 was knocked down by small interfering RNA (siENO1) in ECs, which were then subjected to DS and PS in the step flow channel. ENO1 knockdown resulted in the restoration of the DS-suppressed anti-inflammatory genes such as KLF2 and NOS3, as well as decreases of the DS-induced inflammatory genes CXCL8 and CXCR4 (Fig. 4*C*). In addition, ENO1 knockdown increased the expression of DS-inhibited EC markers CD31 and CDH5, while suppressing the DS-induced mesenchymal markers ADAM15, CDH2, IL6, SMAD3 and TGFB2 (Fig. 4*D*). Immunostaining experiment confirmed that ENO1 knockdown reduced CDH2 expression in the DS region (*SI Appendix*, Fig. S5). We also incubated ECs following ENO1 knockdown with TGF-β and IL-1β. These EndMT stimuli caused mesenchymal transition, indicated by the increases of smooth muscle cell α-actin (α-SMA), SM22α and vimentin (Vim), together with decreases of CD31 and CDH5 (Fig. 4*E*). In contrast, ENO1 knockdown resulted in significant decreases of mesenchymal markers ADAM15, CDH2, IL6, SMAD3 and TGFB2, with concordant increases of the EC markers CD31 and CDH5 (Fig. 4*E*). To validate these results in vivo, we assessed the ENO1 expression in the atherosclerotic lesion at the aorta arch of the ApoE$^{-/-}$ mice. Immunostaining showed that the level of ENO1 was higher in the vWF (von Willebrand factor)-labeled endothelium of the atherosclerotic lesion, in comparison to the nondisease region in the thoracic aorta (Fig. 4*F*). In summary, the results in Fig. 4 suggest that DS up-regulated ENO1 to increase the inflammatory response and mesenchymal transition in endothelium, leading to the atherogenic phenotype.

Discussion

We investigated the responses of cultured HAECs in a step flow channel to both the DS dynamics found at atheroprone sites and the PS dynamics found at atheroprotective sites (Fig. 1*A*). Using this step flow channel, we interrogated the transcriptome of the same monolayer of HAECs subjected to precisely controlled DS and PS simultaneously at the single-cell level, in relation to their functional phenotypes. Our scRNA-seq analyses revealed EC heterogeneity associated with different transcriptomes at these different flow areas in the same flow chamber. Specifically, DS caused EC transition from homeostatic to a proliferative, inflammatory, and atherogenic phenotype (Fig. 2 *E*–*H* and *SI Appendix*, Fig. S3) and promoted EC subpopulations (DS-MLCs) to undergo EndMT (Fig. 3). The DS-induced EndMT involves changes of gene expressions in inflammatory and hypoxic responses, TGF-β signaling, as well as those in metabolic pathways, e.g., glycolysis and lipid synthesis. Among the DEGs, a high level of ENO1 induction was detected in DS-MLCs; pseudotemporal trajectory analysis shows that the expression of ENO1 was positively associated with EndMT progression. Silencing of ENO1 repressed the DS- and TGFβ-regulated inflammatory genes and mesenchymal markers. Furthermore, the expression of ENO1 in the endothelium of atherosclerotic lesions in ApoE$^{-/-}$ mice was significantly higher than that in normal aortas, suggesting a significant role of the DS-induced ENO1 in its proatherogenic effect in the arterial tree. Collectively, these findings indicate that DS induces a transcriptome leading to EndMT and that the DS upregulation of ENO1 may underly the atheroprone flow-induced EC heterogeneity, inflammation, and EndMT.

The paired comparison of the same sets of ECs significantly enhanced the rigor of the experimental design and increased the statistical significance of the data. The DS induced by the step change involves a transverse flow direction that mimics in vivo hemodynamic conditions (24); this is not addressed when ECs are subjected to PS and OS in the conventional parallel plate or cone-and-plate flow channels. DEGs analysis, cell type annotation, and pseudotemporal trajectory analysis indicate that DS promoted EC heterogeneity and plasticity with distinct transcriptomic profiles and functions. Generated from experiments using the step flow channel, these results provide significant insights into the critical roles of mechanical stimuli in regulating EC biology.

ECs in the DS region exhibited greater atherogenic phenotype than those in the PS region, as evidenced by actin fiber disassembly, inflammation, mitochondria fission, mtROS accumulation, and increases of proliferation and mesenchymal markers (Fig. 1). Excessive mitochondrial fission has been linked to mitochondrial dysfunction and mtROS elevation, which are implicated as early events in atherogenesis (36). PS has been reported to enhance EC mitochondrial fusion (37); we have found that DS increased EC mitochondrial fission and mtROS production (Fig. 1 *C* and *D*). Our scRNA-seq DEG assay demonstrated that HIF1A was up-regulated in ECs in response to DS (*SI Appendix*, Fig. S1). Since HIF1A has been found to promote mitochondrial fission and mtROS production (18, 38), our finding suggests that HIF1A may be the upstream regulator for the DS-induced mitochondrial impairment.

EndMT plays a key role in the development of the cardiovascular system and is involved in the pathophysiology of vascular diseases during adulthood such as atherosclerosis (33, 34). Our previous studies employing bulk RNA-seq, RT-PCR, and western blot on ECs subjected uniformly to OS in the parallel-plate chamber showed that the atheroprone flow-induced EndMT is associated with decreases of EC markers and increases of mesenchymal markers (5, 8). These measurements only provide an averaged expression profile across all ECs in response to different flow conditions, but do not identify the distinct transcriptomic profile in subtypes of ECs. Here, we used the SingleR algorithm that references the human primary cell atlas data to perform unbiased annotation of each cell for its cell type assignment. This approach allowed us to identify an EC subpopulation in the DS-clusters that undergoes EndMT (DS-MLC). These DS-MLCs, besides exhibiting the mesenchymal markers, presented the transcriptional signatures associated with inflammation, hypoxia, TGF-β signaling, and metabolic processes. All these biological processes are consistent with the hallmarks involved in the induction of EndMT (32). In addition, KEGG pathway analysis of these DS-MLCs revealed that the most significantly enriched pathways are cellular senescence pathway, fluid shear stress and atherosclerosis, necroptosis, apoptosis, TNF signaling pathway, and TGF-β signaling pathway, which underscore atherosclerotic development (32, 39), reinforcing EndMT occurred in this subpopulation of ECs. Although previous in vivo scRNA-seq studies have generated the transcriptomic data supporting the EndMT process during vascular dysfunction (14, 16, 40, 41), they could not exclude the complexity of multiple cell sources such as the infiltrated immune cells, which may also contribute to mesenchymal transition (42). Thus, the present study reveals the detailed transcriptomic profiles in EC subpopulations undergoing the DS-induced EndMT.

Within the DS-MLC subpopulation identified by our scRNA-seq, ENO1 was one of the top DS-induced genes. ENO1, the multifunctional protein with oncogenic properties, is an emerging molecular target for cancer therapy. In contrast to cancer cell study, however, there are very few reports on ENO1 in vascular biology. Among these limited studies, ENO1 has been implicated in the pathogenesis of pulmonary hypertension (43, 44), and microarray profiling revealed that ENO1 is up-regulated in symptomatic plaques (45). By comparing the effects of DS and PS acting on the same EC population, our scRNA-seq datasets showed that DS induced ENO1 expression in ECs. In reviewing

the published datasets (5, 16), we did find that atheroprone flow (OS/flow disturbance) up-regulates ENO1 (5, 16) (*SI Appendix*, Fig. S6), but its role under DS with respect to EC dysfunction has not been investigated, nor discussed. The current scRNA-seq results identify that ENO1 was predominantly expressed in the DS-MLC subpopulation; this led to our analyses combining cell type annotation and pseudotime trajectory to uncover that the kinetics of ENO1 expression are positively correlated with that of EndMT (Fig. 3 *G*–*J*). Importantly, ENO1-knockdown attenuated the DS-induced EC inflammation and EndMT in vitro (Fig. 4 *C* and *D*). The high levels of ENO1 in ECs under DS in vitro and in atherosclerotic lesions in vivo (Fig. 4*F*) further underscore its role in vascular dysfunction.

Adaptation of EC metabolism is known to play critical roles in the regulation of EndMT (35). Our detailed analysis of the transcriptomic profile in ECs undergoing EndMT revealed an enrichment of metabolic processes including glycolysis and fatty acid metabolism. In addition to the high levels of ENO1, the DS-MLC subpopulation also showed high levels of FASN, a key enzyme in fatty acid synthesis, and several other genes regulating lipogenesis, e.g., FADS2, FADS3, and PTGS1 (Fig. 3*G*). Given that FASN mediates EMT in many cancer cell types and that knockdown of FASN abolished EMT (46), the induction of FASN and other genes promoting lipid synthesis would reinforce EndMT in DS-MLC driven by DS. This is in agreement with our previous studies showing that DS induces a sustained activation of SREBP1, the master transcription factor for lipogenic gene expression (47, 48). Pseudotemporal trajectory analysis showed positive correlations of these genes with EndMT, like that of ENO1 (*SI Appendix*, Fig. S7), suggesting that increased lipogenesis plays a role in DS-induced EndMT. It has been reported that inhibition of fatty acid oxidation is indispensable for TGF-β induction of EndMT (35). However, we did not observe the downregulation of genes related to fatty acid oxidation; it is possible that EndMT induced by chemical vs mechanical stimuli may differ in their effects on the metabolic pathways (49).

Our scRNA-seq studies have generated a comprehensive view of transcriptomes at the single-cell level in response to DS vs. PS. The DS-dependent transcriptomic changes result in endothelial heterogeneity and plasticity, including EndMT. This DS-induced EndMT with distinct gene expressions in inflammatory, hypoxic responses, TGF-β signaling, and metabolic reprogramming (glycolysis and lipid synthesis) would contribute to atherosclerosis. Additionally, the DS-induced ENO1 has been shown to be an essential driver of EndMT. In summary, our current findings provide valuable insights and data resources to better understand the mechanisms of regulation of flow-dependent vascular functions. This can further facilitate the development of effective therapeutic targets or strategies for the prevention and treatment of vascular diseases.

Materials and Methods

HAEC Culture. HAECs purchased from Cell Applications and cultured in medium 199 (M199, Gibco) were supplemented with 10% fetal bovine serum (FBS, Gibco) and Endothelial Cell Growth Medium (Cell Applications). HAECs at passages 4 to 6 were used for the flow experiments, in which the cells were seeded onto fibronectin (50 μg/mL)-coated glass slides (75 × 38 mm; Corning) for 24 h before being subjected to step flow experiments.

Flow System, Chamber Design, and Computational Simulation. The step flow chamber was constructed, and flow patterns were measured as previously described (23). Briefly, disturbed flow (DS) was created by a step expansion of the height of the flow channel in a parallel-plate chamber (Fig. 1*A*). To mimic the physiological condition of pulsatile flow, 1 Hz oscillations with an amplitude of ±20 mL/min were superimposed on the mean flow rate of 60 mL/min, corresponding to a downstream laminar shear stress of 12 ± 4 dynes/cm^2.

Single-cell Isolation and Single-cell Sequencing. After having been subjected to shear flows for 24 h, the ECs collected from the glass slide were disbursed with 0.25% Trypsin-EDTA. The cell debris and large clumps were removed with a cell strainer (50 μm). The cells were suspended in 1× phosphate buffered saline (PBS) with 0.04% bovine serum albumin (BSA), counted, and immediately processed to generate single-cell encapsulation and barcoding into gel beads-in-emulsions by using the 10× Genomics Chromium device following the standard 10× Chromium Single Cell 3′ v3 (10× Genomics Technology) protocols according to the manufacturer's specifications. Subsequently, complementary DNA (cDNA) amplification was performed, and libraries were prepared, followed by Illumina 4000 sequencing with a depth of >100 million reads per sample.

Single-cell RNA-seq Data Analysis. Raw sequencing data were demultiplexed, aligned, and counted by using CellRanger software. The reads were aligned to human UCSC GRch38 reference genome. The alignment results were used to quantify the expression levels of human genes and the generation of gene-barcode matrix. Seurat 4.0.2 version was used to perform gene counts and cell filtration, normalization, dimension reduction, variable gene finding, clustering analysis, and visualization of the clusters by UMAP. Gene counts <200 or >4,000 and mitochondria-unique molecular identifier counts >10% were filtered out for exclusion of noncell or cell aggregates. Among the three independent pairs of PS and DS experiments performed, one set of PS/DS datasets showed more than 85% of cells with >10% mitochondrial unique molecular identifier, hence was not included in further analysis. The two independent PS/DS datasets were integrated with Seurat analyses for normalization, data scaling, gene feature selection, anchor correspondences identification, dimension reduction (canonical correlation analysis), anchor scoring (shared nearest neighbor graphs), and anchor weighting (K weight and visualization of clusters by UMAP). Gene expression was visualized with feature plot, dot plot, violin plot, and heatmaps, which were generated by functions of FeaturePlot, DotPlot, VlnPlot, and DoHeatmap, respectively. DEGs were identified by functions of FindAllMarkers and FindMarkers with Wilcoxon test for significance (adjusted *P* value <0.05) and filtered by average $\log_2$ (fold change) > 0.25. SingleR was applied to perform cell type annotation with human primary cell atlas data reference dataset and single-cell pseudotime trajectory analysis by using Monocle3 with default parameter.

GO Term Analysis and GSEA Analysis. The GO term enrichment analysis was performed using ViSEAGO with multiple comparisons and the whole quail genome as background. All enriched GO terms ($P < 0.01$) were grouped into functional clusters using hierarchical clustering based on Wand's semantic similarity between GO terms representing GO graph topology and Ward's criterion. The ClusterProfiler was used to perform the GSEA enrichment analysis, and GSEA plots were performed using the gseaplot2 function of the enrichplot package. False discovery rate < 0.25 and *P* value < 0.05 were set as the cutoff criteria.

RT-PCR. 1 to 2 μg total RNA of the HAECs collected from the step flow chamber was isolated by using TRIzol (Invitrogen) according to the manufacturer's protocol and then converted to cDNA using the MMLV reverse transcriptase system and oligo-dT primers (Invitrogen). Briefly, total RNA (0.5 to 1 μg, in diethyl pyrocarbonate water) was incubated with 200 U/μL MMLV reverse transcriptase in a buffer containing 20 mM Tris-HCl, 2.5 mM $MgCl_2$, 0.5 mM deoxynucleoside triphosphate mix, 10 mM dithiothreitol, and oligo-$dT_{12\text{-}18}$ (0.5 μg/mL) for 50 min at 37 °C. Reactions were terminated with *Escherichia coli* RNase H (2 U/μL) after 15 min at 70 °C.

Quantitative real-time PCR (qPCR) for mRNA Expression. cDNA from 0.5 to 1 μg total RNA was obtained by using the MMLV Reverse Transcriptase (Invitrogen) as described above. Real-time PCR was performed on a CFX ConnectTM real-time PCR detection system (BioRad). The amplification condition was initiated with denaturation at 95 °C for 10 min, followed by 40 cycles of 95 °C for 10 s, 55 °C for 10 s, and 70 °C for 30 s. mRNA expression was normalized to the expressions of β-actin and GAPDH. For primer sequences, please see *SI Appendix*, Table S2.

Immunofluorescent Staining. For in vitro assays, HAECs were fixed in 4% paraformaldehyde and permeabilized with 0.1% Triton X-100 for 10 min, followed by blocking with 5% BSA. FITC-phalloidin (Invitrogen) was used for F-actin staining and cell morphology analysis. For in vivo assay, immunofluorescence staining was performed on two consecutive sections of paraffin-embedded $ApoE^{-/-}$ mice aortas using antibodies against ENO1, the EC-specific marker vWF, and the VSMC-specific marker α-SMA. DAPI (Sigma) was used for nucleus staining. The images

were taken under an epifluorescence microscope (Olympus IX70) for quantification of cell morphology parameters.

En Face Preparation and Staining. All animal experiments performed in this study were in accordance with NIH guidelines and approved by the Institutional Animal Care and Use Committee of the University of California at San Diego. Mice were euthanized by breathing with 100% carbon dioxide. The carotid arteries were perfusion fixed with 50 mL of lukewarm PBS and 10% formalin. The carotid arteries were carefully dissected, with the adventitia removed, and postfixed in fixative solution for 2 h. The arteries were longitudinally dissected with microdissecting scissors and pinned flatly on a black wax dissection pan. The luminal surfaces of the arteries were immediately blocked with 10% FBS for 1 h, followed by incubation with the designated primary antibodies for ENO1 (1:100; Abcam) and vWF (1:100; Invitrogen) at 4 °C overnight. Alexa Fluor 594–conjugated anti-mouse IgG (1:500; Invitrogen) and Alexa Fluor 488–conjugated anti-rabbit IgG (1:500; Invitrogen) were used as secondary antibodies. The nuclei were costained with DAPI (Sigma) in PBS for 10 min. The sections were spin-dried and mounted with ProLong Gold (Invitrogen) on glass coverslips. The images were obtained using a confocal fluorescence microscope (Olympus FV1000) with 40× oil objective.

Analysis of Mitochondrial Morphology Subtypes. HAECs were fixed in cold methanol for 15 min and then stained with MitoTracker Red (CMXROS, Invitrogen) for 30 min, and DAPI was used for nuclear staining. The images were obtained using a confocal fluorescence microscope (Olympus FV1000) with 60× oil objective. An automatic classification software MicroP (50) was used to characterize the compositions of mitochondrial morphology as globular and tubular subtypes.

mtROS Staining. MtROS was detected in HAECs stained with 10 μM MitoSOX™ Red (Invitrogen) at 37 °C for 30 min. After staining, the HAECs were washed, and images were acquired under a fluorescence microscope with a 60× oil objective.

Transfection. HAECs were grown to 70% confluence and transfected with specific siRNA for ENO1 (Invitrogen) at 20 nM using RNAiMAX (Invitrogen), according to the manufacturer's protocol. After transfection for 24 h, HAECs were subjected to PS and DS in the step flow chamber for knockdown experiments.

EndMT Assay. For the induction of EndMT, HAECs were cultured in the EC culture medium supplemented with TGF-β2 (10 ng/mL, R&D systems) and IL-1β (10 ng/mL, R&D systems) for 48 h. Then, RNA was isolated and assayed for gene expression by qPCR.

Statistical Analysis. Unpaired and 2-tailed Student *t* tests were applied to analyze and compare data between two groups. Data were presented as mean ± SEM using GraphPad Prism 8 software. Experimental repeats in each group are specified in the figure legends. $P < 0.05$ was considered statistically significant.

Data, Materials, and Software Availability. The scRNA-seq data are available for reproducing the results. The FASTQ files generated from the current scRNA-seq study have been deposited at the NCBI BioProject repository (accession number PRJNA1033703) and will be available upon publication (51). The authors declare that all R scripts used to process data are available from the corresponding author, if requested.

ACKNOWLEDGMENTS. We wish to thank Dr. Kun Zhang in the Department of Bioengineering, UCSD (University of California San Diego), for insightful advice and discussions for data analyses and Dr. Jian Kang in the Department of Medicine, UCSD, for her technical assistance in flow channel experiments. This work was supported in part by NIH grants R01HL108735 (to Z.B.C., S.S., J.Y.-J.S., and S.C.), R01HL106579 (to S.S., J.Y.-J.S., and S.C.), R01HL145170 (to Z.B.C.), HL121365 (to S.C.), R21AG075450 (to M.H.), and American Heart Association Career Development Award 859625 (to M.H.).

Author affiliations: [a]Department of Bioengineering, University of California at San Diego, La Jolla, CA 92093; [b]Institute of Engineering in Medicine, University of California, San Diego, La Jolla, CA 92093; [c]Division of Cardiology, Department of Medicine, University of California, San Diego, La Jolla, CA 92093; [d]Department of Diabetes Complications and Metabolism, Beckman Research Institute, City of Hope, Duarte, CA 91010; and [e]San Diego Supercomputer Center, University of California at San Diego, La Jolla, CA 92093

Author contributions: L.-J.C., J.Y.-S.L., M.H., Z.B.C., S.S., J.Y.-J.S., and S.C. designed research; L.-J.C. and P.N. performed research; L.-J.C., J.Y.-S.L., and M.H. analyzed data; and L.-J.C., J.Y.-S.L., M.H., Z.B.C., S.S., J.Y.-J.S., and S.C. wrote the paper.

1. J. J. Chiu, S. Chien, Effects of disturbed flow on vascular endothelium: Pathophysiological basis and clinical perspectives. *Physiol. Rev.* **91**, 327–387 (2011).
2. P. Nigro, J. Abe, B. C. Berk, Flow shear stress and atherosclerosis: A matter of site specificity. *Antioxid. Redox Signal* **15**, 1405–1414 (2011).
3. J. Zhou, Y. S. Li, S. Chien, Shear stress-initiated signaling and its regulation of endothelial function. *Arterioscler. Thromb. Vasc. Biol.* **34**, 2191–2198 (2014).
4. C. Souilhol *et al.*, Endothelial responses to shear stress in atherosclerosis: A novel role for developmental genes. *Nat. Rev. Cardiol.* **17**, 52–63 (2020).
5. N. E. Ajami *et al.*, Systems biology analysis of longitudinal functional response of endothelial cells to shear stress. *Proc. Natl. Acad. Sci. U.S.A.* **114**, 10990–10995 (2017).
6. M. He *et al.*, Atheroprotective flow upregulates ITPR3 (Inositol 1,4,5-Trisphosphate Receptor 3) in vascular endothelium via KLF4 (Kruppel-Like Factor 4)-mediated histone modifications. *Arterioscler. Thromb. Vasc. Biol.* **39**, 902–914 (2019).
7. T. S. Huang *et al.*, LINC00341 exerts an anti-inflammatory effect on endothelial cells by repressing VCAM1. *Physiol. Genom.* **49**, 339–345 (2017).
8. B. Lai *et al.*, Atheroprone flow enhances the endothelial-to-mesenchymal transition. *Am. J. Physiol. Heart Circ. Physiol.* **315**, H1293–H1303 (2018).
9. Y. Miao *et al.*, Enhancer-associated long non-coding RNA LEENE regulates endothelial nitric oxide synthase and endothelial function. *Nat. Commun.* **9**, 292 (2018).
10. A. S. Kalluri *et al.*, Single-cell analysis of the normal mouse aorta reveals functionally distinct endothelial cell populations. *Circulation* **140**, 147–163 (2019).
11. J. Kalucka *et al.*, Single-cell transcriptome atlas of murine endothelial cells. *Cell* **180**, 764–779.e20 (2020).
12. D. T. Paik *et al.*, Single-cell RNA sequencing unveils unique transcriptomic signatures of organ-specific endothelial cells. *Circulation* **142**, 1848–1862 (2020).
13. S. W. Lukowski *et al.*, Single-cell transcriptional profiling of aortic endothelium identifies a hierarchy from endovascular progenitors to differentiated cells. *Cell Rep.* **27**, 2748–2758.e3 (2019).
14. C. K. Cheng *et al.*, SOX4 is a novel phenotypic regulator of endothelial cells in atherosclerosis revealed by single-cell analysis. *J. Adv. Res.* **43**, 187–203 (2023).
15. F. Li *et al.*, Single-cell RNA-seq reveals cellular heterogeneity of mouse carotid artery under disturbed flow. *Cell Death Discov.* **7**, 180 (2021).
16. A. Andueza *et al.*, Endothelial reprogramming by disturbed flow revealed by single-cell RNA and chromatin accessibility study. *Cell Rep.* **33**, 108491 (2020).
17. S. W. S. Leung, Y. Shi, The glycolytic process in endothelial cells and its implications. *Acta Pharmacol. Sin.* **43**, 251–259 (2022).
18. D. Wu *et al.*, HIF-1alpha is required for disturbed flow-induced metabolic reprogramming in human and porcine vascular endothelium. *Elife* **6**, e25217 (2017).
19. Y. Han *et al.*, Roles of KLF4 and AMPK in the inhibition of glycolysis by pulsatile shear stress in endothelial cells. *Proc. Natl. Acad. Sci. U.S.A.* **118**, e2103982118 (2021).
20. F. A. Almaguel, T. W. Sanchez, G. L. Ortiz-Hernandez, C. A. Casiano, Alpha-enolase: Emerging tumor-associated antigen, cancer biomarker, and oncotherapeutic target. *Front. Genet.* **11**, 614726 (2020).
21. C. K. Huang, Y. Sun, L. Lv, Y. Ping, ENO1 and cancer. *Mol. Ther. Oncolyt.* **24**, 288–298 (2022).
22. J. J. Chiu *et al.*, Analysis of the effect of disturbed flow on monocytic adhesion to endothelial cells. *J. Biomech.* **36**, 1883–1895 (2003).
23. P. P. Hsu *et al.*, Effects of flow patterns on endothelial cell migration into a zone of mechanical denudation. *Biochem. Biophys. Res. Commun.* **285**, 751–759 (2001).
24. Y. Mohamied *et al.*, Change of direction in the biomechanics of atherosclerosis. *Ann. Biomed. Eng.* **43**, 16–25 (2015).
25. I. A. Tamargo, K. I. Baek, Y. Kim, C. Park, H. Jo, Flow-induced reprogramming of endothelial cells in atherosclerosis. *Nat. Rev. Cardiol.* **20**, 738–753 (2023), 10.1038/s41569-023-00883-1.
26. B. Braam *et al.*, Nitric oxide-dependent and nitric oxide-independent transcriptional responses to high shear stress in endothelial cells. *Hypertension* **45**, 672–680 (2005).
27. C. W. Ni *et al.*, Discovery of novel mechanosensitive genes in vivo using mouse carotid artery endothelium exposed to disturbed flow. *Blood* **116**, e66–73 (2010).
28. A. Brionne, A. Juanchich, C. Hennequet-Antier, ViSEAGO: A Bioconductor package for clustering biological functions using Gene Ontology and semantic similarity. *BioData Min.* **12**, 16 (2019).
29. S. Nestorowa *et al.*, A single-cell resolution map of mouse hematopoietic stem and progenitor cell differentiation. *Blood* **128**, e20-31 (2016).
30. Z. A. Clarke *et al.*, Tutorial: Guidelines for annotating single-cell transcriptomic maps using automated and manual methods. *Nat. Protoc.* **16**, 2749–2764 (2021).
31. D. Aran *et al.*, Reference-based analysis of lung single-cell sequencing reveals a transitional profibrotic macrophage. *Nat. Immunol.* **20**, 163–172 (2019).
32. C. Souilhol, M. C. Harmsen, P. C. Evans, G. Krenning, Endothelial–mesenchymal transition in atherosclerosis. *Cardiovasc. Res.* **114**, 565–577 (2018).
33. S. Islam *et al.*, The mechanobiology of endothelial-to-mesenchymal transition in cardiovascular disease. *Front. Physiol.* **12**, 734215 (2021).
34. P. Y. Chen *et al.*, Endothelial-to-mesenchymal transition drives atherosclerosis progression. *J. Clin. Invest.* **125**, 4514–4528 (2015).
35. J. Xiong *et al.*, A metabolic basis for endothelial-to-mesenchymal transition. *Mol. Cell* **69**, 689–698.e7 (2018).
36. E. Bouhamida *et al.*, The interplay of hypoxia signaling on mitochondrial dysfunction and inflammation in cardiovascular diseases and cancer: From molecular mechanisms to therapeutic approaches. *Biology (Basel)* **11**, 300 (2022).
37. L. H. Wu, H. C. Chang, P. C. Ting, D. L. Wang, Laminar shear stress promotes mitochondrial homeostasis in endothelial cells. *J. Cell Physiol.* **233**, 5058–5069 (2018).
38. G. Marsboom *et al.*, Dynamin-related protein 1-mediated mitochondrial mitotic fission permits hyperproliferation of vascular smooth muscle cells and offers a novel therapeutic target in pulmonary hypertension. *Circ Res.* **110**, 1484–1497 (2012).

39. J. L. M. Bjorkegren, A. J. Lusis, Atherosclerosis: Recent developments. *Cell* **185**, 1630–1645 (2022).
40. L. S. Tombor *et al.*, Single cell sequencing reveals endothelial plasticity with transient mesenchymal activation after myocardial infarction. *Nat. Commun.* **12**, 681 (2021).
41. M. Wu, Y. Wu, S. Tang, J. Huang, Y. Wu, Single-cell RNA-seq uncovers distinct pathways and genes in endothelial cells during atherosclerosis progression. *Front. Mol. Biosci.* **10**, 1176267 (2023).
42. S. Piera-Velazquez, S. A. Jimenez, Endothelial to mesenchymal transition: Role in physiology and in the pathogenesis of human diseases. *Physiol. Rev.* **99**, 1281–1324 (2019).
43. Y. Shi *et al.*, Targeting endothelial ENO1 (Alpha-Enolase) -PI3K-Akt-mTOR axis alleviates hypoxic pulmonary hypertension. *Hypertension* **80**, 1035–1047 (2023).
44. J. Dai *et al.*, Alpha-enolase regulates the malignant phenotype of pulmonary artery smooth muscle cells via the AMPK-Akt pathway. *Nat. Commun.* **9**, 3850 (2018).
45. L. Perisic *et al.*, Profiling of atherosclerotic lesions by gene and tissue microarrays reveals PCSK6 as a novel protease in unstable carotid atherosclerosis. *Arterioscler. Thromb. Vasc. Biol.* **33**, 2432–2443 (2013).
46. J. Li *et al.*, Fatty acid synthase mediates the epithelial-mesenchymal transition of breast cancer cells. *Int. J. Biol. Sci.* **10**, 171–180 (2014).
47. Y. Liu *et al.*, Shear stress activation of SREBP1 in endothelial cells is mediated by integrins. *Arterioscler. Thromb. Vasc. Biol.* **22**, 76–81 (2002).
48. M. S. Brown, J. L. Goldstein, The SREBP pathway: Regulation of cholesterol metabolism by proteolysis of a membrane-bound transcription factor. *Cell* **89**, 331–340 (1997).
49. J. Zhou *et al.*, Force-specific activation of Smad1/5 regulates vascular endothelial cell cycle progression in response to disturbed flow. *Proc. Natl. Acad. Sci. U.S.A.* **109**, 7770–7775 (2012).
50. J. Y. Peng *et al.*, Automatic morphological subtyping reveals new roles of caspases in mitochondrial dynamics. *PLoS Comput. Biol.* **7**, e1002212 (2011).
51. L. J. Chen *et al.*, Data from "Single-Cell RNA Sequencing Unveils Unique Transcriptomic Signatures of Endothelial Cells and Role of ENO1 in Response to Disturbed Flow." National Center for Biotechnology Information. https://dataview.ncbi.nlm.nih.gov/object/PRJNA1033703?reviewer=p296dg91uam9kl7oakenspcsbq. Deposited 30 October 2023.